

## INNER ORBITS IN HIERARCHICAL TRIPLE SYSTEMS FROM THE CHARA ARRAY. I. V819 Her B

DAVID P. O'BRIEN<sup>1</sup>, HAROLD A. MCALISTER<sup>1</sup>, DEEPAK RAGHAVAN<sup>1</sup>, TABETHA S. BOYAJIAN<sup>1</sup>, THEO A. TEN BRUMMELAAR<sup>2</sup>,  
JUDIT STURMANN<sup>2</sup>, LASZLO STURMANN<sup>2</sup>, NILS H. TURNER<sup>2</sup>, AND STEPHEN RIDGWAY<sup>3</sup>

<sup>1</sup> Center for High Angular Resolution Astronomy, Department of Physics and Astronomy, Georgia State University, P.O. Box 3969, Atlanta, GA 30302-3969, USA;  
obrien@chara.gsu.edu, hal@chara.gsu.edu, raghavan@chara.gsu.edu, tabetha@chara.gsu.edu

<sup>2</sup> CHARA Array, Mount Wilson Observatory, Mount Wilson, CA 91023, USA; theo@chara-array.org, judit@chara-array.org,  
sturmann@chara-array.org, nils@chara-array.org

<sup>3</sup> National Optical Astronomy Observatory, P.O. Box 26732, Tucson, AZ 85726-6732, USA; sridgway@noao.edu

Received 2010 February 18; accepted 2010 December 13; published 2011 January 26

### ABSTRACT

We employ the wide component of a triple system to calibrate the interferometric visibility of the inner, short-period orbit in the case of V819 Her. The orbit for V819 Her B was thereby derived by performing a  $\chi^2$  fit to interferometric visibility measurements from observations of fringe packets at the CHARA Array. Comparing this orbit to that of V819 Her AB (the wider orbit in this hierarchical triple system), the mutual inclination was found to be  $33^\circ.5 \pm 9^\circ.3$ , consistent with observations of other triple systems. Also, due to the presence of an evolved component in the system, the age of the system can be estimated to be  $1.9 \text{ Gyr} \pm 1.1 \text{ Gyr}$ .

*Key words:* binaries: close – techniques: interferometric

### 1. INTRODUCTION

As first described by Dyck et al. (1995), the angular separation of the components of a binary star may be sufficiently wide to reveal non-overlapping or separated fringe packets when observed in a fringe-scanning mode by a long-baseline interferometer. In certain triple star systems, the orbital geometry of the three components may be such that one of the separated fringe packet pairs corresponds to the wide component whereas the other packet is associated with the inner, short-period system whose resolution is targeted. This approach utilizes the observed visibility of the wide component to calibrate instrumental and atmospheric effects on the interferometric visibility of the close binary. Standard interferometric practice calls for the observation of a calibrator star, selected as close as possible to the target star, in a bracketed sequence before and after observations of the target. In triple systems where the angular separation between the close binary and the wide component is relatively small (on the order of 80 milliarcsec (mas)), all components can be observed nearly simultaneously during a single scan through interferometric delay. This reduces the offset in time between the target and calibrator from minutes to a few tenths of a second and in position from degrees to a few tens of mas. In principle, this provides for a more accurate calibration than the standard method. The calibrated visibilities of the inner orbit can then be used to determine the visual orbital elements of the close binary system.

We have identified roughly 30 triple systems amenable to this approach. These objects typically consist of a long-period system whose visual orbital elements have been measured by speckle interferometry and a short-period system possessing a spectroscopic orbit. Once the visual orbit of the short-period system is determined from long-baseline interferometry, the mutual inclination of the two orbits comprising the triple system can be calculated. A resolved spectroscopic binary provides the angular semimajor axis, the orbital inclination, and the nodal longitude to the standard set of spectroscopic elements. However, the longitude of the node possesses a  $180^\circ$  ambiguity. In general, visual orbits for both the long-period and

short-period components in triple systems are rare (Fekel 1981). Triple systems with visual orbits for the close binary usually have wide orbits with periods too long for study. On the other hand, triple systems in which the wide orbit can be determined visually usually have unresolvable close orbits. Thus, the number of systems accessible to this approach is modest. However, the long baselines of the CHARA Array enable the determination of visual orbits for the close binaries of triple systems with existing visual orbits for the wide component.

One such system, V819 Her (HD 157482), is the first target for which an orbit has been determined by this separated fringe packet approach. This object consists of a giant star (G8 III) orbiting a pair of F dwarfs (F2V + F8V). The wide component's orbit is eccentric ( $e = 0.673$ ), with a period of 5.5 years and a semimajor axis of 75 mas, while the close binary orbit is circular, with a period of 2.2296334 days (Scarfe et al. 1994). The evolved star is the brightest component of the system, so it is designated as A, while the close binary components are designated as Ba and Bb, with Ba being the brighter of the two F stars. The close binary is a single-lined spectroscopic binary, with the fainter component undetected in the spectrum. However, it is also an eclipsing system, so Bb has been characterized by its effect on the light curve (Van Hamme et al. 1994).

This system has been well-studied through the years. Consistent orbital solutions have been derived for the wide orbit through speckle interferometry (Scarfe et al. 1994) and differential astrometry (Muterspaugh et al. 2006). Examination of the light curve of the close binary has resulted in eclipsing orbits (Van Hamme et al. 1994; Wasson et al. 1994). An orbital solution for the close binary and a value for the unambiguous mutual inclination have also been derived by Muterspaugh et al. (2008) using differential astrometry obtained from long-baseline interferometry. The approach used in this paper has resulted in a similar orbital solution to the one derived by Muterspaugh et al. (2008), thus allowing for a demonstration of the reliability of our method. Although separated fringe packets have been observed several times for astrometric purposes and searches for previously unknown stellar companions (Baguolo et al. 2006;

**Table 1**  
Observed Visibility Measurements

Epoch (MJD)	B (m)	$\psi$ (deg)	$V_{A,o}$	$\sigma V_{A,o}$	$V_{B,o}$	$\sigma V_{B,o}$	$N$
53948.357	330.5	163.8	0.2185	0.0146	0.0750	0.0040	3
53948.369	330.3	161.1	0.2291	0.0154	0.0782	0.0055	2
54288.219	245.3	25.7	0.2310	0.0111	0.0836	0.0043	3
54605.383	278.5	143.0	0.3022	0.0171	0.0846	0.0039	1
54650.294	330.5	16.9	0.1903	0.0107	0.0683	0.0038	4
54650.307	330.6	14.0	0.1965	0.0058	0.0673	0.0025	4
54650.320	330.7	11.1	0.1998	0.0076	0.0655	0.0040	4
54650.333	330.7	8.2	0.1895	0.0088	0.0602	0.0040	4
54650.346	330.6	5.1	0.1650	0.0090	0.0532	0.0041	4
54651.289	330.4	17.6	0.2619	0.0076	0.0967	0.0067	3
54651.307	330.6	13.5	0.2702	0.0077	0.0943	0.0051	4
54651.325	330.7	9.2	0.2422	0.0114	0.0733	0.0061	3
54651.337	330.6	6.6	0.2417	0.0071	0.0588	0.0037	4
54651.348	330.6	3.8	0.2341	0.0098	0.0583	0.0031	3
54651.359	330.6	1.2	0.2300	0.0054	0.0626	0.0028	4
54662.297	330.7	8.9	0.1777	0.0082	0.0636	0.0058	3
54662.309	330.6	6.1	0.1829	0.0100	0.0674	0.0047	3
54662.330	330.6	0.9	0.1516	0.0089	0.0444	0.0043	2
54662.339	330.6	178.9	0.1446	0.0081	0.0429	0.0042	3
54663.276	330.6	13.0	0.1472	0.0086	0.0516	0.0026	3
54663.286	330.7	10.7	0.1481	0.0156	0.0554	0.0046	3
54663.298	330.7	8.0	0.1509	0.0107	0.0579	0.0039	4
54933.510	277.1	136.9	0.3897	0.0121	0.0899	0.0036	3

**Notes.** The “B” in Columns 2 and 3 represents baseline, while the “B” in Columns 6 and 7 represents component B in the triple system.

Farrington 2008; Raghavan 2009), this is the first attempt to employ them in the visibility calibration process.

## 2. OBSERVATIONS AND DATA REDUCTION

### 2.1. Observations

The small separation of the wide AB system, coupled with the system’s moderate magnitude difference, makes V819 Her a perfect target for employing separated fringe packets in the calibration process. The system was observed at the CHARA Array on several different nights between 2005 June and 2009 April. All observations were made in the  $K'$  band ( $2.13 \mu\text{m}$ ) using the “CHARA Classic” beam combiner. The majority of these observations were taken using the 331 m baseline between the CHARA Array’s S1 and E1 telescopes. Long baselines are required to resolve the two fringe packets in most cases, thus this longest baseline is preferred. The remaining observations were taken with CHARA’s 278 m (S1-W1) and 250 m (S2-W1) baselines. A thorough description of the layout of the CHARA Array, the CHARA Classic beam combiner, standard observing practices, and data reduction procedures is given by ten Brummelaar et al. (2005).

The data obtained for orbit fitting are presented in Table 1. In order to reduce computing time and scatter in the data, several sets (roughly 5 minutes each) of data have been averaged together. The epoch given in Table 1 is the mid-observation epoch of all data sets represented by that point. The final column of Table 1 indicates the number of data sets included in each point.

### 2.2. Initial Data Processing

Each data file consists of roughly 200 recorded fringe scans recorded at a frequency of 150 Hz. When searching for a

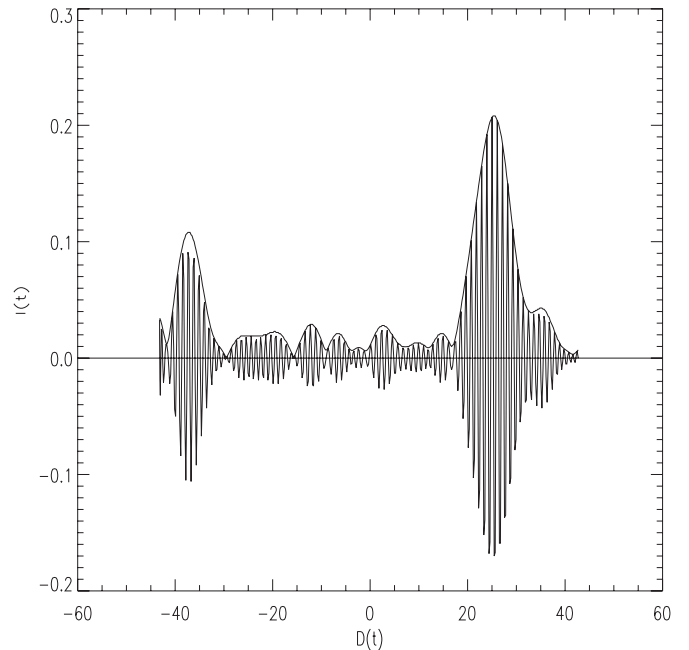


**Figure 1.** Sample data scan plus envelope from 2006 August 1. This is a plot of intensity vs. the position of the fringe scanning mirror in microns as a function of time. Several subsequent figures shall use the same axes.

secondary fringe packet in a data scan, it is often more useful to look at the envelope of the scan, rather than the scan itself, an example of which is shown in Figure 1.

For V819 Her, the primary fringe packet is almost always visible and prominent, but the secondary fringe packet can be more troublesome. Shift-and-add addition of many scans very effectively smooths the atmospheric noise within the individual scans, leaving the two fringe packets clearly visible. Instances of poor seeing can cause the secondary packet to move relative to the position of the primary packet from scan to scan, so that in the shift-and-added envelope, the secondary packet would be smeared out and not visible. Thus, data must be meticulously examined in order to confirm or deny the existence of the secondary packet. Figure 2 shows a shift-and-added envelope for an entire data set. The primary packet is prominent, and the secondary packet is clearly visible to the right of the primary.

Once the existence of the secondary packet in a data set has been established, each data scan must be examined, and criteria for the rejection of scans must be established. In order to avoid biasing the results with low signal-to-noise data, 40% of the scans in each data set are rejected based on their low signal-to-noise ratios. A relative signal-to-noise ratio measurement is calculated for each scan by dividing the peak of a scan’s power spectrum by the integrated area under the power spectrum from 300 to 325 Hz (a band outside the position of the fringe (150 Hz) in the frequency domain). The separation between the two fringe packets in each scan must also be considered. If the separation measurement for a particular scan is outside of  $3\sigma$  of the mean of all scans in the set, then one or both of the fringe packets has been misidentified, most likely due to noise peaks. These scans are rejected. A related consideration is the position of the fringe packets. The positions of the primary and secondary packets should be relatively consistent between successive scans in a data set. To measure the level of consistency, the position of the primary fringe packet in a scan is compared to the mean of the primary’s position in the two previous and the two successive scans. If the position differs from that mean by more than  $27 \mu\text{m}$

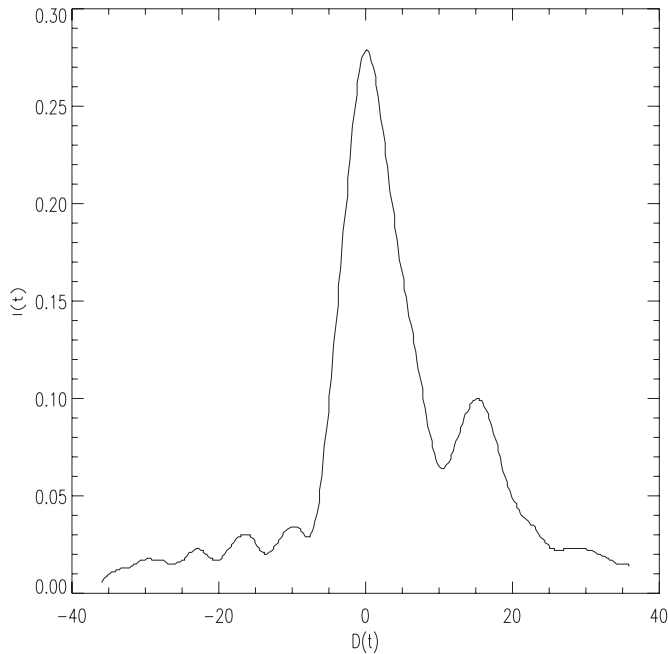


**Figure 2.** Shift-and-added envelope for a data set taken on 2008 July 15.

(one third of the overall scan length), the primary fringe packet is considered to be misidentified, and the scan is rejected. This process is repeated for the secondary fringe packet. Finally, all scans are visually inspected to make sure that the fringe packets have not drifted outside of the scan range. Due to either piston error or poor seeing, the fringe packets may drift out of the scan range during observation. Scans such as these must be rejected as well. Typically, after all rejection criteria have been satisfied, roughly 50% of the data scans remain.

### 2.3. Fringe Fitting

Fringe fitting is performed on the selected fringe scans in order to obtain visibilities for both fringe packets. Fringe fitting is performed in one of two ways, depending on the separation between the two fringe packets. If the fringe packets are relatively far apart, the two packets should be fit separately. When the packets are close together, such that they are overlapping, the two packets should be fit simultaneously.

The fringe equation giving intensity as a function of time (Benson et al. 1995) to be fit is

$$I(t) = \phi_0 \frac{\sin(\pi \phi_1 \phi_2 t)}{\pi \phi_1 \phi_2 t} \cos(2\pi \phi_2 \phi_3 t + \phi_4), \quad (1)$$

where  $\phi_0$  is the interferometric visibility,  $\phi_1$  represents the inverse of the coherence length ( $(\frac{\lambda^2}{\Delta\lambda})^{-1}$ , where  $\lambda$  and  $\Delta\lambda$  are the effective wavelength and bandwidth of observation, respectively),  $\phi_2$  is the group velocity of the fringe scanning mirror,  $\phi_3$  is the wave number, and  $\phi_4$  is a phase shift introduced by atmospheric piston fluctuations.

Although we nominally know  $\lambda$  and  $\Delta\lambda$  from the manufacturer's testing of our  $K$ -band filter, we chose to keep those parameters in the solution because of a small bias that is introduced by the transmissive and reflectance properties of the atmosphere, mirror surfaces, and optical windows as well as the detector spectral response across the  $K$  passband. Also, the group velocity is not constant during a scan. The fringe scanning mirror is attached to a moving cart that acts to equalize the optical path

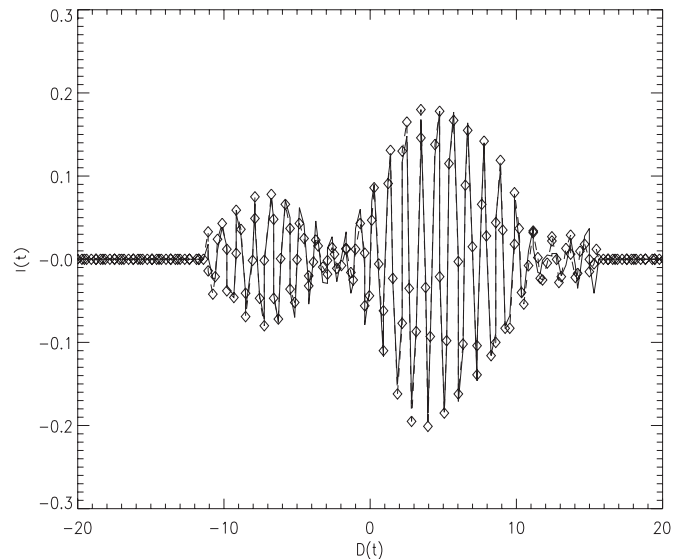


**Figure 3.** Typical simultaneously fit separated fringe packet. The diamonds represent individual data points and the solid line represents the fit to the fringe packet. As a contrast to the fit, the dashed line simply connects the data points.

length of the two telescopes as a target moves across the sky. The cart's movement introduces an acceleration term into the movement of the fringe scanning mirror, so the velocity must be treated as a free parameter as well. In general, the standard deviation of the fitted values for both the group velocity and  $\lambda$  among all non-rejected scans in a data set are both less than 3%. The standard deviation of  $\Delta\lambda$  is larger, at roughly 15%.

The five-parameter fit is applied after initial "guess" values are assigned to the  $\phi$ -parameters. Three different fringe fits, centered on the highest amplitude individual fringe in the packet and on its two nearest neighbors, are performed on each packet. The fit with the smallest standard deviation of its residuals is accepted as the best fringe fit. Only  $\phi_0$ , the fringe visibility, is used in further data reduction. When the fringe packets are far enough apart, they should be fit separately, resulting in a  $\phi_0$  value for each packet, which represents the visibility of the respective packet. We hereinafter denote visibility by the symbol  $V$  and drop the reference to its source  $\phi_0$  in the fringe fitting process.

When fringe packets are close together, or even overlapping, fitting the fringe packets separately is insufficient in obtaining the correct parameters for the system. The presence of side lobes associated with the fringe packets will result in an enhancement or diminution of the effective fringe amplitudes depending upon the phase shift between the two. To account for this effect, it is necessary to fit the fringe packets simultaneously, using a modified version of Equation (1) that includes two additional parameters: the visibility of a second packet and the separation between the two. An example of a simultaneous fit is given in Figure 3.

Although in theory simultaneous fitting could be used in any case, it does not work as well for widely separated fringe packets. This process involves fitting several hundred noise points in between the primary and secondary packets. In many cases, noise peaks can be relatively large in amplitude compared to the secondary packet. The resulting fits have large residuals in the area of the secondary packet, so it is doubtful that the fit is accurately representing the visibility of this object. For this reason, it is preferable to use the separate, rather than simultaneous, fitting approach when dealing with widely separated fringe packets.

The result of the fringe fitting, whether separate or simultaneous, is a pair of visibilities for each data scan. The final primary visibility for each data set is the average of the primary visibilities of all scans that are not weighted to zero. Likewise, the final secondary visibility is the average of all secondary visibilities for scans not weighted zero. These averaged results represent the observed visibility for a single data set, which must undergo a few additional corrections before the true visibility of the target can be obtained.

#### 2.4. Calibration

Calibration is the next step in obtaining the binary star visibilities that will be used in orbit fitting. The observed visibility of the calibrator, A, must be used to calibrate the observed visibility of the binary, B, to obtain the true visibility of the binary. The true visibility is defined here as the intrinsic visibility of the system. In an ideal case, a calibrator would be an unresolved, non-variable, single star with a  $K'$ -band magnitude equal to the target. In this case, the ratio of the true visibilities ( $\frac{V_A}{V_B}$ ) would be equal to the ratio of the observed visibilities ( $\frac{V_{A,o}}{V_{B,o}}$ ). In the case of V819 Her, the calibrator is a giant that is roughly 1 mag brighter than the close binary (Scarfe et al. 1994). The ratio of observed visibilities is thus affected by a factor of  $\beta_{\text{wide}}$ , the luminosity ratio between the target and calibrator. The relationship between observed and true visibilities is

$$\frac{V_A}{V_B} = \beta_{\text{wide}} \left( \frac{V_{A,o}}{V_{B,o}} \right). \quad (2)$$

The true visibility of the calibrator can be calculated using the equation for the visibility of a single star with angular diameter  $\Theta$  (generally determined by either fitting a spectral energy distribution or calculating based on spectral type and parallax, but here adopted from Scarfe et al. 1994), observed at wavelength  $\lambda$  with baseline  $B$ :

$$V_A = \frac{2 * J_1\left(\frac{\pi\Theta_A B}{\lambda}\right)}{\left(\frac{\pi\Theta_A B}{\lambda}\right)}, \quad (3)$$

where  $J_1$  is the first-order Bessel function.

The value of  $\beta_{\text{wide}}$  is left as a free parameter in the orbit fit, as discussed in the next section. True visibilities of the close binary,  $V_B$ , are calculated for the best-fit value of  $\beta_{\text{wide}}$  and presented in Table 2.

### 3. ORBIT FITTING PROCEDURE

Calibrated visibilities obtained by single-baseline observations unfortunately cannot be broken down into the instant angular separation ( $\rho$ ) and binary position angle ( $\theta$ ), as there are an infinite number of combinations of separation and position angle that will produce a given visibility. Therefore, the orbit fitting program used to produce this orbit must be based on a  $\chi^2$  fit of the observed visibilities to the equation for a binary star visibility:

$$V_B = (1 + \beta_{\text{close}})^{-1} \left[ V_{\text{Ba}}^2 + \beta_{\text{close}}^2 V_{\text{Bb}}^2 + 2V_{\text{Ba}}V_{\text{Bb}}\beta_{\text{close}} \cos\left(\frac{2\pi\rho B}{\lambda} \cos(\psi - \theta)\right) \right]^{0.5}, \quad (4)$$

where  $V_{\text{Ba}}$  and  $V_{\text{Bb}}$  are the respective single star visibilities of the primary and secondary components of the binary, which

**Table 2**  
Observed and True Visibilities of Components A and B

Epoch	$\frac{V_{A,o}}{V_{B,o}}$	$V_A$	$V_B$
53948.357	2.913	0.8924	0.8594
53948.369	2.930	0.8926	0.8547
54288.219	2.763	0.9398	0.9541
54605.383	3.572	0.9228	0.7247
54650.294	2.786	0.8924	0.8986
54650.307	2.920	0.8923	0.8574
54650.320	3.050	0.8923	0.8207
54650.333	3.148	0.8923	0.7953
54650.346	3.102	0.8923	0.8071
54651.289	2.708	0.8925	0.9245
54651.307	2.865	0.8923	0.8737
54651.325	3.304	0.8923	0.7576
54651.337	4.111	0.8923	0.6090
54651.348	4.015	0.8923	0.6234
54651.359	3.674	0.8923	0.6814
54662.297	2.794	0.8923	0.8960
54662.309	2.714	0.8923	0.9225
54662.330	3.414	0.8923	0.7332
54662.339	3.371	0.8923	0.7427
54663.276	2.853	0.8923	0.8775
54663.286	2.673	0.8923	0.9364
54663.298	2.606	0.8923	0.9605
54933.510	4.335	0.9235	0.5977

**Notes.** The value of  $\beta_{\text{wide}} = 0.356$  used here is from the orbit fit calculated in Section 5.

are calculated using Equation (3).  $\beta_{\text{close}}$  is the luminosity ratio between the two components of the close binary,  $B$  is the baseline of observation,  $\lambda$  is the wavelength of observation,  $\psi$  is the position angle of the baseline of observation projected onto the sky,  $\rho$  is the angular separation between the primary and secondary, and  $\theta$  is the position angle of the binary.

Several parameters of the close binary orbit have been fixed in the fitting routine based on previously published information. The eccentricity ( $e$ ) and longitude of periastron ( $\omega$ ) can be fixed at zero based on the deduction of a circular orbit (Scarfe et al. 1994). The period ( $P$ ) of the close binary has been established by several sources (Scarfe et al. 1994; Van Hamme et al. 1994; Wasson et al. 1994; Muterspaugh et al. 2006). Angular diameters for the two stars are also fixed by the radii and parallax derived by Scarfe et al. (1994), but because the diameters are so small, ( $<0.5$  mas) they have very little effect on fringe visibility. Finally, the value  $\alpha \sin i$  has been adopted from the spectroscopy of Scarfe et al. (1994) and the parallax.

The variable parameters for the fit are semimajor axis ( $\alpha$ ), inclination ( $i$ ), epoch of periastron ( $T_0$ ), nodal position angle ( $\Omega$ ), the magnitude difference between Ba and Bb ( $\Delta m_{\text{close}}$ ), and the magnitude difference between A and B ( $\Delta m_{\text{wide}}$ ). In circular orbits, the epoch of periastron is replaced by the epoch of the ascending node ( $T_{\text{node}}$ ) (Heintz 1978).

The orbit fitting code is a slightly modified version of that of Raghavan et al. (2009). The program is first run to explore possible solutions within reasonable lower and upper limits to the free parameters. A higher-resolution grid search of the best-fit parameter space then converges on the final solution. In each step through the multi-parameter grid, the current set of orbital parameters is used to calculate the angular separation  $\rho$  and position angle  $\theta$  of the binary at each epoch of observation.  $\rho$  and  $\theta$  are then used to determine the visibility at each epoch by Equation (4). These modeled visibilities are then compared to

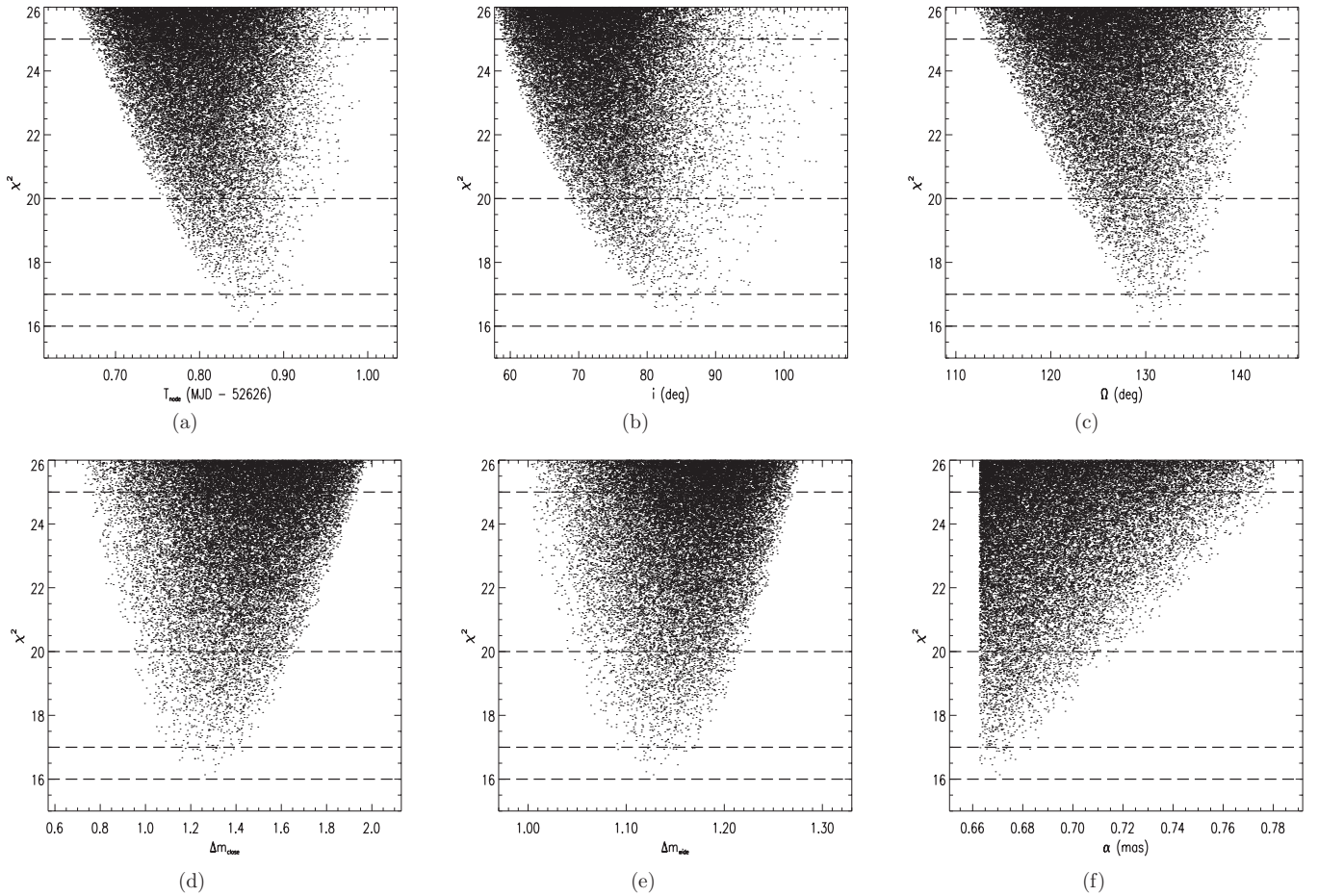


**Figure 4.**  $\chi^2$  plots for variable elements in the orbit fit. The “wall” on the left-hand side of the  $x$ -axis in (f) is due to the fact that  $\alpha \sin i$  is fixed in the orbit fitting. The inclination is thus dependent on the randomly chosen semimajor axis. At values of  $\alpha < \alpha \sin i$ , the calculation of  $i$  will lead to an arcsine of a value greater than 1, giving a non-physical result.

the true visibilities derived by Equation (2) and a  $\chi^2$  value is returned. The set of orbital parameters that result in the minimum  $\chi^2$  is adopted as the best-fit solution.

The Raghavan et al. (2009) method of determining uncertainties is adopted here. Several hundred thousand iterations of the orbit fit are run for randomly selected values of the orbital parameters. Using the  $\chi^2$  value for each iteration, a multi-dimensional  $\chi^2$  volume is created. When this volume is projected onto an individual parameter axis, a plot such as those in Figure 4 is created, where each point represents the  $\chi^2$  value of one iteration of the orbit fit. These points are plotted on the  $x$ -axis at the position of the parameter that represents the randomly selected value for that particular iteration of the fit. The levels above the minimum  $\chi^2$  that mark the  $1\sigma$ ,  $2\sigma$ , and  $3\sigma$  confidence levels can be determined by the table on p. 555 of Press et al. (1986). According to that source, those confidence levels are located at 1.00, 4.00, and 9.00 above the minimum  $\chi^2$  when all parameters are varied simultaneously. The horizontal dashed lines in Figure 4 represent those confidence levels. The uncertainties on the orbital parameters are determined by the intersection of the  $1\sigma$  dashed line with the outer edges of the collection of points.

The final orbit solution is given in Table 3. As seen from the table, these results are based on a fit with six free parameters and six constraints. The errors on the visibilities derived in Section 2 and presented in Table 1 led to an overestimation of the errors on the orbital parameters. These errors on the visibilities were scaled downward until a reduced  $\chi^2$  of 1.00 was achieved. These

results are in reasonable agreement with previously published information, specifically the orbit derived by Muterspaugh et al. (2008), which is also presented in the table. Most of the orbital elements are within the  $1\sigma$  error bars of Muterspaugh et al. (2008). The exception is the inclination, for which there is a  $1.3\sigma$  deviation from the value of Muterspaugh et al. (2008). The resulting best-fit solution to the visibilities is shown in Figure 5.

## 4. FUNDAMENTAL PROPERTIES

### 4.1. Mutual Inclination

One important result from this study is the mutual inclination ( $\Phi$ ) that has been calculated from the orientations of the wide and close orbits. The mutual inclination in a triple system is the angle between the planes of the wide orbit and the close orbit, given by Fekel (1981):

$$\cos \Phi = \cos i_{\text{wide}} \cos i_{\text{close}} + \sin i_{\text{wide}} \sin i_{\text{close}} \cos(\Omega_{\text{wide}} - \Omega_{\text{close}}), \quad (5)$$

where  $i_{\text{wide}}$  and  $i_{\text{close}}$  are the inclinations and  $\Omega_{\text{wide}}$  and  $\Omega_{\text{close}}$  are the nodal position angles of the wide and close orbits. The quantity  $\Phi$  has long been an item of astronomical interest because of its relation to the conditions under which triple systems form (Sterzik & Tokovinin 2002). Initial understanding of the mutual inclination suggested that all triple systems should be coplanar ( $\Phi = 0^\circ$ ), but more recent results have shown that this is not the case.

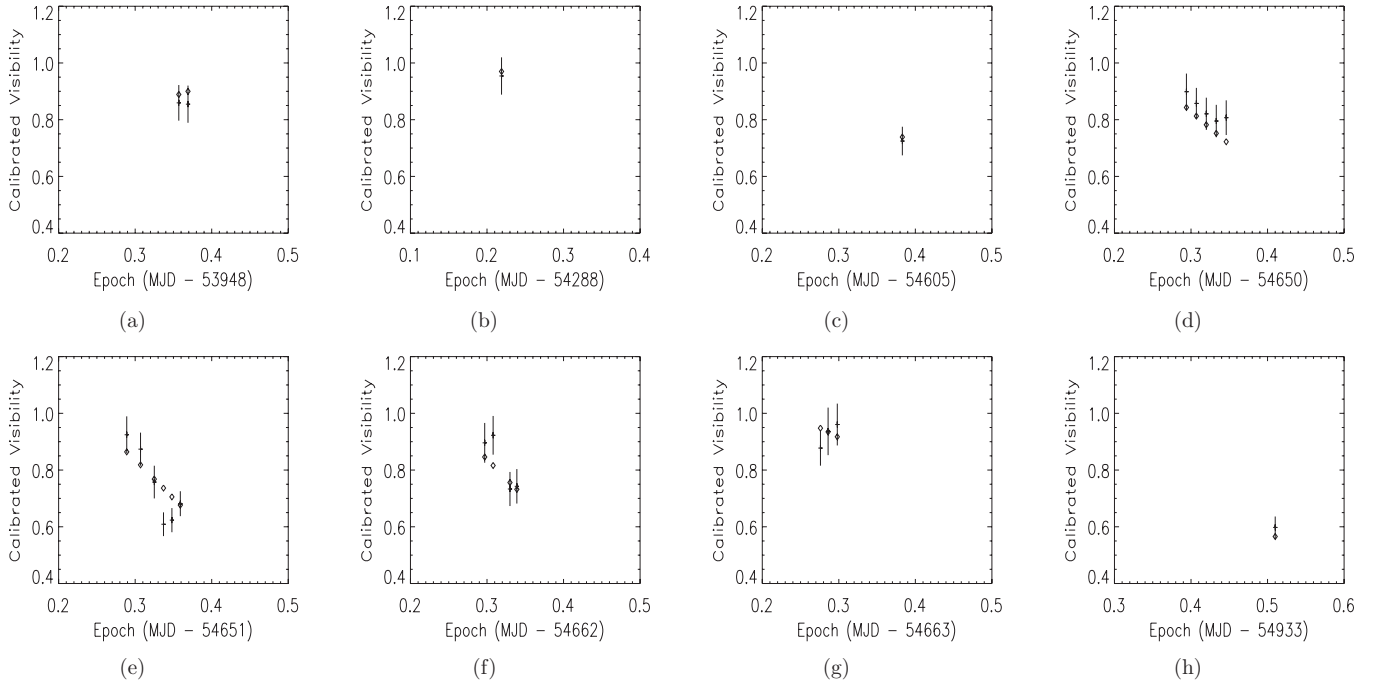


Figure 5. Optimal orbit fit for the eight different nights of data.

Table 3  
Orbital Elements Derived from Minimum Chi-squared Fit

Element	Value	Muterspaugh et al. (2008)
Fixed elements		
$P$ (day)	$2.2296334 \pm 1.6 \times 10^{-6}$	$2.2296330 \pm 1.9 \times 10^{-6}$
$\alpha \sin i$ (mas)	$0.6625 \pm 0.0230$	
$e$	0	$0.0041 \pm 0.0033$
$\omega$ (deg)	0	$227 \pm 47$
$\Theta_p$ (mas)	$0.126 \pm 0.002$	
$\Theta_s$ (mas)	$0.085 \pm 0.002$	
Varied elements		
$T_{\text{node}}$ (MJD)	$52626.872 \pm 0.054$	$52627.17 \pm 0.29$
$\alpha$ (mas)	$0.6631 \pm 0.0221$	$0.6657 \pm 0.0058$
$i$ (deg)	$87.6 \pm 9.7$	$80.70 \pm 0.38$
$\Omega$ (deg)	$131.3 \pm 4.0$	$131.1 \pm 4.1$
$\Delta m_{\text{close}}$	$1.24 \pm 0.21$	$1.38 \pm 0.14$
$\Delta m_{\text{wide}}$	$1.128 \pm 0.050$	
Reduced $\chi^2$	1.00	

Note. Muterspaugh et al. (2008) orbital elements are presented for comparison.

The attempts of Bodenheimer (1978) to model the formation of multiple systems have predicted orbital coplanarity at all stages of development. However, Fekel (1981), using statistics of several observed multiple systems, concluded that at least a third of multiple systems are definitely not coplanar. Fekel defined coplanarity in this study as

$$\Phi < 15^\circ. \quad (6)$$

Fekel only had spectroscopic orbits for the inner orbits in his systems so he could not calculate  $\Phi$  directly. Since the term  $\cos(\Omega_{\text{wide}} - \Omega_{\text{close}})$  must be between 0 and  $\pi$ , a minimum  $\Phi$  can be calculated based on the orbits' inclinations. Seven of the twenty-one multiple systems considered by Fekel had a  $\Phi_{\text{min}}$  that did not satisfy condition (6), and thus were deemed non-coplanar. The remaining 14 systems could not be categorized as either coplanar or non-coplanar without visual orbits (Fekel 1981).

A study by Sterzik & Tokovinin (2002) further addressed the issue of coplanarity. Sterzik & Tokovinin (2002) determined an average value of the mutual inclination using data from the Multiple Star Catalog (Tokovinin 1997). For a sample of 14 triple systems, the calculated average is  $\langle \Phi \rangle = 67^\circ \pm 9^\circ$  (Sterzik & Tokovinin 2002). This suggests a strong tendency against coplanarity. However, this result is very preliminary. The sample size of the study is small and the standard deviation of  $\langle \Phi \rangle$  is large ( $\sigma = 64^\circ$ ). Also, 3 of the 14 systems meet the requirements for coplanarity according to condition (6). Furthermore, for 11 of these 14 systems, the value for either  $\Omega_{\text{wide}}$  and  $\Omega_{\text{close}}$  possesses an ambiguity of  $180^\circ$ , so the mutual inclination is also ambiguous. Clearly, more systems must be added to these statistics to get a better idea of the mutual inclinations in triple systems.

In addition to using multiple systems for which the orbits are known, Sterzik & Tokovinin (2002) also performed extensive modeling of triple systems. This modeling involved following  $N$ -body collapsing cloud simulations until stable triple system configurations are reached, then performing statistical analysis on the mutual inclinations of the resulting systems. The most important initial conditions are the shape of the initial cloud, its rotational energy, and its virial status. The initial conditions that best match observations are an axis ratio of 10:1, a rotational energy of 10% of the overall gravitational energy of the system, and no random kinetic energy. These conditions give an average mutual inclination of  $\langle \Phi \rangle = 63^\circ \pm 5^\circ$ , compared to the value  $\langle \Phi \rangle = 67^\circ \pm 9^\circ$  from observations. This result matches observations better than the previous modeling efforts by Bodenheimer (1978), which suggest coplanarity at all fragmentation stages. Examination of other simulations with different initial conditions shows a strong tendency against coplanarity in all cases (Sterzik & Tokovinin 2002).

The approach used in this paper provides the visual orbit of V819 Her B and directly yields  $\Omega_{\text{close}}$ . However, the derived value suffers from the  $180^\circ$  ambiguity discussed above. This leads to two possible values of the mutual inclination, as shown

**Table 4**  
Mutual Inclination

Element	Value (deg)	
$i_{\text{wide}}$	$56.2 \pm 0.4$	
$i_{\text{close}}$	$87.6 \pm 9.7$	
$\Omega_{\text{wide}}$	$143.7 \pm 0.3$	
Ambiguous values		
$\Omega_{\text{close}}$	$131.3 \pm 4.0$	$311.3 \pm 4.0$
$\Phi$	$33.5 \pm 9.3$	$142.0 \pm 9.4$

**Table 5**  
Unambiguous Mutual Inclinations

Star	$\Phi$	Reference
V819 Her	$33.5 \pm 8.7$	This paper
	$26.3 \pm 1.5$	Muterspaugh et al. (2008)
$\kappa$ Peg	$43.4 \pm 3.0$	Muterspaugh et al. (2008)
$\eta$ Vir	$30.8 \pm 1.3$	Hummel et al. (2003)
$\epsilon$ Hya	39.4	Heintz (1996)
$\zeta$ UMa	132.1	Heintz (1996)
Algol	$95 \pm 3$	Csizmadia et al. (2009)
	$98.8 \pm 4.9$	Lestrade et al. (1993)
		Pan et al. (1993)

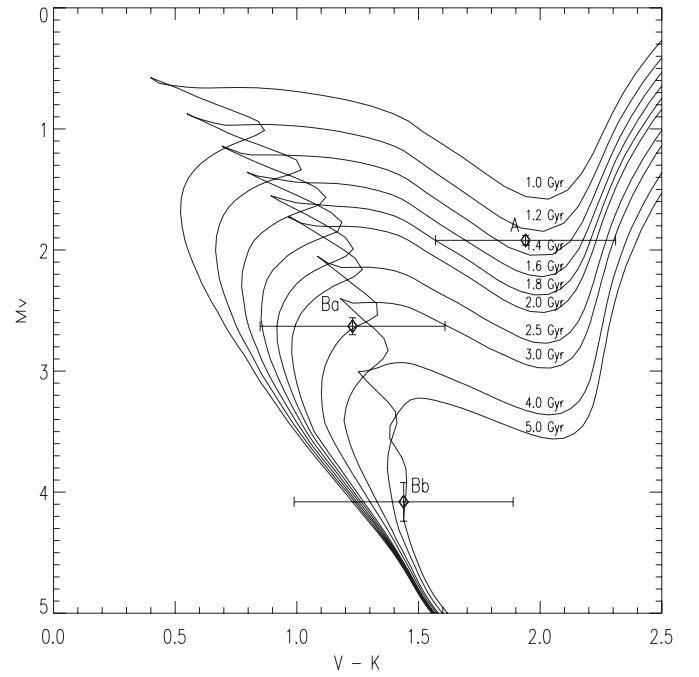
**Table 6**  
Masses

Element	Value
$\pi$ (mas)	$14.5 \pm 0.2$
$\alpha$ (mas)	$0.6631 \pm 0.0221$
$a$ (AU)	$0.04573 \pm 0.00163$
$P$ (days)	$2.2296334 \pm 1.9 \times 10^{-6}$
$q$	$0.725 \pm 0.010$
$M_B$ ( $M_{\odot}$ )	$2.566 \pm 0.274$
$M_{\text{Ba}}$ ( $M_{\odot}$ )	$1.488 \pm 0.181$
$M_{\text{Bb}}$ ( $M_{\odot}$ )	$1.079 \pm 0.148$

in Table 4. The findings from Muterspaugh et al. (2008), whose differential astrometry observations can resolve the ambiguity in  $\Omega_{\text{close}}$ , suggest that, of the two values of  $\Phi$  presented in Table 4, the correct value is  $33^{\circ}5 \pm 9^{\circ}3$ . In addition to V819 Her, unambiguous mutual inclinations have been calculated for five other systems. These systems are listed in Table 5. This table has been adapted from Table 6 in Muterspaugh et al. (2006). None of these six systems can be considered coplanar according to the criteria by Fekel (1981). The results presented here on V819 Her B, along with the information on the other targets in Table 4, and the studies by Fekel (1981) and Sterzik & Tokovinin (2002), strongly argue against coplanarity.

#### 4.2. Mass Estimates

The derivation of the semimajor axis of V819 Her B, when combined with the mass ratio given by the spectroscopy of Scarfe et al. (1994), allows for the calculation of the individual


**Figure 6.**  $M_V$  vs.  $V - K$  for V819 Her components along with  $Y^2$  isochrones for  $m_{\text{AB}} = 3.839$ .

masses of the system. Those masses, along with all values needed to calculate them, are given in Table 6. The results are reasonable for the spectral types of these stars, and are in very good agreement with the masses derived by Muterspaugh et al. (2008) and Scarfe et al. (1994).

#### 4.3. Age

Due to the presence of the evolved component (V819 Her A), it is possible to estimate the age of V819 Her. Combining the overall  $K$  magnitude ( $m_{\text{AB}}$ ) of the system with  $V$  magnitudes from Scarfe et al. (1994) and the derived values of  $\Delta m_{\text{close}}$  and  $\Delta m_{\text{wide}}$ , the three components of the system can be plotted on an H-R diagram. The Two Micron All Sky Survey value of the overall  $K$  magnitude ( $m_{\text{AB}} = 3.839 \pm 0.368$ ) is adopted for the system (Skrutskie et al. 2006). Table 7 shows the derived  $K$  magnitudes for each of the components.

Figure 6 shows the components plotted against Yonsei-Yale isochrones (Demarque et al. 2004) for solar mixtures. Component A lies between the isochrones for 1.2 and 1.4 Gyr, while component Ba lies roughly at 2.5 Gyr. Component Bb is not considered in the age determination, as its proximity to the main sequence causes decent agreement with virtually all of the plotted isochrones. Based on this information, along with the large uncertainties in the  $K$  magnitudes, the estimated age of this system is  $1.9 \pm 1.1$  Gyr. This value is very rough, and is somewhat different than the age of  $1.5 \pm 0.3$  Gyr given by Scarfe et al. (1994).

**Table 7**  
Magnitudes of Components

	AB	B	A	Ba	Bb
$M_V$			$1.92 \pm 0.04$	$2.63 \pm 0.07$	$4.08 \pm 0.16$
$m_V$			$6.11 \pm 0.05$	$6.82 \pm 0.08$	$8.27 \pm 0.16$
$m_K$	$3.839 \pm 0.368$	$5.30 \pm 0.37$	$4.17 \pm 0.37$	$5.60 \pm 0.37$	$6.84 \pm 0.42$
$V - K$			$1.94 \pm 0.37$	$1.22 \pm 0.38$	$1.43 \pm 0.45$

**Note.**  $V$  magnitudes are taken from Scarfe et al. (1994).

## 5. CONCLUSION

We have shown how the very high angular resolution of the CHARA Array can be used to determine the inner orbits of triple systems. The nearly simultaneous observation of the wide, long-period components has been demonstrated to provide the means for calibrating interferometric visibility of the close, short-period system in the case of the hierarchical triple system V819 Her. The orbit and mutual inclination derived using this method compare favorably with those found by Muterspaugh et al. (2008), while the age of V819 Her determined here is in reasonable agreement with Scarfe et al. (1994). An important result of the derivation of a visual orbit for a close binary in a triple system is the quantity  $\Phi$ , the mutual inclination of the system. This quantity can be helpful in determining the initial conditions of the gas clouds where these systems form (Sterzik & Tokovinin 2002). The average mutual inclination calculated by Sterzik & Tokovinin (2002) is based on a small number of systems, and more orbits are needed to better determine the distribution of mutual inclinations in nature and the formation processes that contribute to that distribution. This paper is the first in a series that will examine the inner orbits of multiple systems in order to further increase understanding of mutual inclination.

We thank the staff of the CHARA Array for their assistance in the completion of this research. The CHARA Array operators, P. J. Goldfinger and Christopher Farrington, have been very helpful in the acquisition of all data used in this paper. We also thank Dr. Matthew Muterspaugh, Dr. Brian Mason, and Dr. Andrei Tokovinin for their correspondence with us. Dr. Tokovinin's Multiple Star Catalog (MSC) has been the main reference tool for this research. Other vital reference tools over the years include the SIMBAD Astronomical Database, the NASA Astrophysical Data System Digital Library, the Vizier Catalogue Service, the 9th Catalogue of Spectroscopic Binary Orbits, the 4th Catalog of Interferometric Measurements of

Binary Stars, and the Washington Double Star Catalog. We have also made use of the Two-Micron All Sky Survey while conducting our research. Research at the CHARA Array is supported by the National Science Foundation through NSF Grant AST 09-08253 and by the College of Arts and Sciences at Georgia State University.

## REFERENCES

- Bagnuolo, W. G., et al. 2006, *AJ*, 131, 2695  
 Benson, J. A., Dyck, H. M., & Howell, R. R. 1995, *Appl. Opt.*, 34, 51  
 Bodenheimer, P. 1978, *ApJ*, 224, 488  
 Csizmadia, S., et al. 2009, *ApJ*, 705, 436  
 Demarque, P., Woo, J., Kim, Y., & Yi, S. K. 2004, *ApJS*, 155, 667  
 Dyck, H. M., Benson, J. A., & Schloerb, F. P. 1995, *AJ*, 110, 1433  
 Farrington, C. 2008, PhD thesis, Georgia State Univ.  
 Farrington, C., et al. 2010, *AJ*, 139, 2308  
 Fekel, F. C. 1981, *ApJ*, 246, 879  
 Heintz, W. D. 1978, *Double Stars* (Geophysics and Astrophysics Monographs, Vol. 15; Dordrecht: Reidel), 32  
 Heintz, W. D. 1996, *AJ*, 111, 408  
 Hummel, C. A., et al. 2003, *AJ*, 125, 2630  
 Lane, B. F., & Muterspaugh, M. W. 2004, *ApJ*, 601, 1129  
 Lestrade, J., Phillips, R. B., Hodges, M. W., & Preston, R. A. 1993, *ApJ*, 410, 808  
 McAlister, H. A., et al. 2005, *ApJ*, 628, 439  
 Muterspaugh, M. W., Lane, B. F., Konacki, M., Burke, B. F., Colavita, M. M., Kulkarni, S. R., & Shao, M. 2006, *A&A*, 446, 723  
 Muterspaugh, M. W., et al. 2008, *AJ*, 135, 766  
 Pan, X., Shao, M., & Colavita, M. M. 1993, *ApJ*, 413, 129  
 Press, W. H., Flannery, B. P., Teukolsky, S. A., & Vetterling, W. T. 1986, *Numerical Recipes in C: The Art of Scientific Computing* (Cambridge: Cambridge Univ. Press)  
 Raghavan, D. 2009, PhD thesis, Georgia State Univ.  
 Raghavan, D., et al. 2009, *ApJ*, 690, 394  
 Scarfe, C. D., Barlow, D. J., Fekel, F. C., Rees, R. F., Lyons, R. W., Bolton, C. T., McAlister, H. A., & Hartkopf, W. I. 1994, *AJ*, 107, 1529  
 Skrutskie, M. F., et al. 2006, *AJ*, 131, 1163  
 Sterzik, M. F., & Tokovinin, A. A. 2002, *A&A*, 384, 1030  
 ten Brummelaar, T. A., et al. 2005, *ApJ*, 628, 453  
 Tokovinin, A. A. 1997, *A&AS*, 124, 75  
 Van Hamme, W. V., et al. 1994, *AJ*, 107, 1521  
 Wasson, R., et al. 1994, *AJ*, 107, 1514